A Numerical Study of the Role of Humidity in the Updraft Driven by Moist Slantwise Convection

VALDIR INNOCENTINI

Instituto Nacional de Pesquisas Espaciais, São José dos Campos, São Paulo, Brazil

ERNESTO DOS SANTOS CAETANO NETO

Instituto de Pesquisas Meteorológicas, UNESP Bauru, São Paulo, Brazil

(Manuscript received 22 April 1991, in final form 22 August 1991)

ABSTRACT

A hydrostatic numerical model with simple microphysical parameterization is used to simulate moist slantwise convection (MSC) in an archetypal initial condition free of other kinds of instability. The numerical experiments are designed to explore the roles of rain evaporation and the spatial distribution of humidity on the evolution of the unstable motion.

The simulations show that the necessary condition of instability $q_e < 0$ (equivalent Ertel potential vorticity) becomes less negative in the region where the slanted updraft and downdraft develop. Potential upright instability is generated above the updraft and also below it in the colder sector.

The updraft resembles an ageostrophic streak of 200 km perpendicular to the thermal wind vector and drifts slowly into the warmer sector with a velocity of 4.5 km h^{-1}, while the parcels near the surface in this sector move toward the updraft. The results indicate the occurrence of a weak low-level jet ahead of the updraft along the thermal wind vector and also a strong high-level jet in the colder sector.

It is found that the surface acts to decrease the value of q_e in the colder region in a shallow layer, although this is not essential in the updraft maintenance. Instead, two conditions play important roles in its maintenance: 1) rain evaporation below the updraft and 2) moist atmosphere on the warm side of the updraft. The rainwater evaporation drives an unstable slantwise downdraft into the warm sector and increases the convergence at low levels, maintaining the slanted updraft active for many hours.

The difficulty in triggering the unstable motion with a small initial perturbation suggests that MSC is perhaps unlikely to occur in nature without a coupled forcing, such as frontogenetical forcing or convective buoyant instability.

1. Introduction

The development of observational techniques using radar and aircraft in meteorology revealed details in extratropical cyclones not provided by early conceptual models. Cunningham (1951) observed a quite heterogeneous cloud structure within a deepening cyclone over Massachusetts. Since then, many observational programs have been designed to characterize the embedded precipitation patterns associated with these systems. Most of them have documented convective midlatitude precipitation organized in lines parallel to the fronts and with horizontal scales around a few hundred kilometers (e.g., Elliot and Hovind 1964, 1965; Nozumi and Arakawa 1968; Austin and Houze 1972; Browning and Harrold 1969; Browning and Pardoe 1973; Houze et al. 1976; Hobbs 1978).

The theory of conditional symmetric instability (CSI) has been evoked as a possible explanation of rainbands seen in the mesoscale range in a baroclinic basic flow. Bennetts and Sharp (1982) examined the CSI criterion in several cases of extratropical cyclones in which the necessary condition for CSI was satisfied. The radars displayed rainbands in 80% of them. Also, several observational studies have described situations with simultaneous occurrence of CSI, or weak conditional symmetric stability (CSS), and other forcing mechanisms. Sanders and Bosart (1985) examined a case of a heavy snowstorm where weak CSS and frontogenetical forcing were identified. Apparently the precipitation was caused by the frontogenetical forcing, and the weak CSS in the warmer air sector contributed in concentrating the ascending motion in a narrow region, enhancing the precipitation. Jascourt et al. (1988) studied a case of five bands separated by clear-air descending motion detected in satellite pictures. They suggested that the upright buoyant instability was modulated by the mesoscale circulation associated with weak dry symmetric stability.

Corresponding author address: Dr. Valdir Innocentini, Instituto Nacional de Pesquisas Espaciais, CPTEC, Av.dos Astronautas, 1758, Caixa Postal 515, Sao Jose dos Campos-SP 12201, Brazil.

Although research results support the hypothesis that CSI plays an important role in the organization of mesoscale rainbands associated with extratropical cyclones, the understanding of several aspects of this mechanism concerning the ideal conditions necessary to maintain active slantwise motion for many hours seems to be very poor. A numerical model, due to its advantages in controlling parameters and quantifying physical processes, is a powerful research tool. Theoretical models like that of Xu (1984) are in general suggestive, but cannot describe CSI properly due to analytical barriers inherent to the nonlinear nature of condensation and evaporation. Bennetts and Hoskins (1979, hereafter BH) carried out numerical simulations of CSI in a nonlinear model in which the water vapor and rainwater were not explicitly included. The heating was specified by a function that depends on the upward velocity and the geometric height. Despite the model's simplicity, the simulations showed an ascending slanted motion concentrated in a narrow region surrounded by two broad and slow descending motions. However, the evaporative effects should have been included in order to describe the descending motion properly, since this mechanism may affect in some way the ascending motion. Recently, Innocentini (1986) and Saitoh and Tanaka (1987, 1988; hereafter ST87, ST88) incorporated a Kessler-type microphysical parameterization in a hydrostatic and nonhydrostatic model, respectively, including explicitly water vapor, cloud, and rainwater. In ST87 the initial condition was obtained by adjusting the equivalent virtual temperature horizontal gradient to a prescribed constant velocity vertical shear, and the condition equivalent Richardson number less than 1 (also a necessary condition of CSI) was controlled by the water vapor amount. The horizontal and vertical grid lengths were 2 and 0.5 km, respectively. Like BH, they also showed that the slantwise updraft induces a convectively unstable midtropospheric layer. Further, they showed that evaporative processes in the rain area below the updraft increase the mass convergence at low levels feeding the updraft.

The present paper investigates several aspects of CSI not discussed earlier. We employ a numerical model for an idealized atmosphere initially free of convective buoyant instability and frontogenetical forcing. Emphasis will be put on delineating the relative importance of rain evaporation, generation of the necessary condition for CSI at low levels, and the role of initial humidity distribution in maintaining the slantwise updraft. The efficiency in releasing slantwise convective available potential energy (SCAPE), defined as the potential energy available for conversion into kinetic energy (Emanuel 1983b), will be calculated. The evolution of equivalent Ertel potential vorticity q_e and other kinds of instabilities (buoyant, symmetric, and inertial) due to the unstable motion will also be examined. In contrast to ST87 the model adopted is hydrostatic with a vertical grid length of 300 m and a horizontal grid length of 14 km, with water substance represented in three stages (vapor, cloud, and rain) and very simple microphysics. As will be shown later, potential upright buoyant instability is generated in several regions, but its triggering is prevented by the descending motion. Thus, it seems unnecessary to simulate CSI in a nonhydrostatic model, except in ST88 simulations where a large supply of water vapor placed at low levels enables upright instability to be triggered in earlier stages of integration where there is no descending motion.

An attempt will be made to obtain an archetypal initial condition. It is designed so that the atmosphere is saturated throughout the domain (except near the boundaries). Unlike in ST87, regions with weaker potential stability to upright convection on the warm side near the boundaries are avoided, as are horizontal gradients of q_e. This prevents the existence of particular regions where the symmetric rolls would be preferred to develop or move away.

Sanders and Bosart (1985) and Emanuel (1983a) showed cases of moving and intensifying cyclones over eastern North America. From the Mexican Gulf position in relation to the synoptic situations depicted, we infer that advections of warm moist air in the warmer sector and cold dry air in the colder sector might have played important roles. In view of these studies, we will reduce the humidity in some sectors of the domain and study its effect on the strength and characteristics of the updraft motion. The objective is to point out that not only is the coupling of CSI with frontogenetical forcing or upright instability at low levels relevant to the development and maintenance of slantwise convection, but so is the availability of moist parcels on the warmer side of the domain. The discussion will be supported by a trajectory analysis of some selected parcels, to detect which parcels are feeding the updraft.

A short review of symmetric instability theories is provided in section 2 emphasizing the remarkable conceptual importance of the inclusion of water substance on the downdraft. The model formulation is presented in section 3, the numerical results and discussions in section 4, and the most significant conclusions are summarized in section 5.

2. Review of symmetric instability theories

This short review is not intended to be complete, but only to point out the main distinctions among dry, conditional, and moist symmetric instabilities. More detailed descriptions of the first two theories are given by BH.

a. Dry symmetric instability (DSI)

Probably DSI was introduced into meteorology by Solberg (1936), referring to a kind of dynamic instability as inertial instability along a surface of constant

potential temperature. Bennets and Hoskins show that the criterion for this instability is the Richardson number $\mathrm{Ri} < f/\eta$, where f is the Coriolis parameter and η is the vertical component of absolute vorticity. The resulting unstable motion has zero phase velocity and no structure along the thermal wind vector. Equivalent to this criterion is the Ertel potential vorticity q negative, $q \equiv \tilde{\eta} \cdot \nabla\theta)/\rho$, where ρ is the density, θ is the potential temperature, ∇ is the three-dimensional gradient operator, and $\tilde{\eta}$ is the three-dimensional absolute vorticity vector. It is easy to show that an atmosphere with $0 < \mathrm{Ri} < f/\eta$ in geostrophic balance must have θ surfaces steeper than M surfaces ($M \equiv fx + V_g$, where x is the axis perpendicular to the thermal wind vector and V_g the geostrophic velocity).

From the Lagrangian point of view, M and θ are conservative quantities when the spatial derivative along the thermal wind vector, friction terms, and perturbation of pressure are neglected (Emanuel 1983b). Under the condition $0 < \mathrm{Ri} < f/\eta$, a parcel moving along a path oriented between its original M and θ surfaces will accelerate away from its initial position. The parcel is unstable for either upward or downward displacements. However, $\mathrm{Ri} < f/\eta$ is rarely found in the atmosphere on a horizontal scale greater than 100 km, except in a very shallow layer near the surface, which prompted BH to include latent heat release in this theory.

b. Conditional symmetric instability (CSI)

To our knowledge, the first reference to CSI was given by Sawyer (1949). In his comments about the inertial instability on θ surfaces, referring to Solberg (1936), he noted that its criterion of instability seems to be rarely satisfied in frontal regions, and wrote

> however since the air is saturated, it is more appropriate to use surfaces of constant equivalent potential temperature for ascending fluid elements . . . the ascending currents would remain saturated but descending fluid elements would ultimately become unsaturated (unless within the rain area) and descending under dry adiabatic would not experience the same instability.

Following his suggestion, the effective static stability is reduced by latent heat release.

For a parcel to be unstable, the θ_e surfaces of equivalent potential temperature (or wet-bulb potential temperature) must be steeper than the M surfaces by arguments similar to those used for DSI. This means that in CSI the equivalent Ertel potential vorticity q_e must be negative, $q_e \equiv (\tilde{\eta} \cdot \nabla\theta_e)/\rho$. Alternatively, the equivalent Richardson number Ri_e must satisfy the relation

$$\mathrm{Ri}_e \equiv \frac{g}{\theta} \frac{\partial\theta_e/\partial z}{(\partial V_g/\partial z)^2} < \frac{f}{\eta} \frac{\partial\theta_e/\partial x}{\partial\theta/\partial x}.$$

The Lagrangian rate of change of q_e is given by

$$\frac{Dq_e}{Dt} = \frac{\tilde{\eta}}{\rho} \cdot \nabla S_{\Theta e} + \frac{\nabla\theta_e}{\rho} \cdot (\nabla \times \mathbf{S}_m) - \frac{g}{\rho\theta} (\mathbf{k} \times \nabla\theta) \cdot \nabla\theta_e, \quad (1)$$

where $\mathbf{S}_m$ and $S_{\Theta e}$ represent sources of momentum and heat other than heat release. Unlike q, not only sources and sinks of momentum and heat can modify the sign of q_e. The understanding of the last term on the right-hand side of (1), hereafter q_r, becomes easier by observing that it is proportional to

$$-\frac{\partial \mathbf{V}_g}{\partial z} \cdot \nabla\theta_e,$$

and its contribution will be nonzero only if there is a vertical shear in the wind component parallel to $\nabla\theta_e$. In a saturated atmosphere, obviously $q_r = 0$. For an unsaturated case, q_r is nonzero provided there is a nonhomogeneous distribution of water vapor mixing ratio along the thermal wind vector, changing the value of $\partial\theta_e/\partial z$. Thus, q_e is increased by q_r if the atmosphere becomes moister at high levels or drier at low levels due to the geostrophic wind advection.

c. Moist slantwise convection (MSC)

The criterion of CSI is actually a generalization of the DSI with θ_e replacing θ for an ascending parcel. For descending motion, θ must be the conservative property considered, and unless $q < 0$, the descending motion is stable. Xu (1984), in an analytical study of CSI, divided the domain into distinct regions, alternating the conservative property in each one, according to upward and downward motion. He was able to show that the linear criterion of instability in an inviscid flow is still $q_e < 0$. However, in order to make the system of equations analytically tractable, he (also BH) assumes that parcels are always ready to release heat. Obviously, a single parcel that descends with θ constant and releases heat immediately when it experiences an ascending motion is not conserving moist static energy. This premise is violating the first law of thermodynamics. The explicit inclusion of water vapor removes this difficulty.

Another limitation in CSI can be noted in the numerical results by BH. The motion obtained is characterized by a narrow slanted updraft between two broader, slowly descending motions. As pointed out by Sawyer (1949), the descending motion would become unsaturated, and beneath the updraft, evaporation of rain could make the descending parcels unstable by the CSI criterion. We define MSC as a flow satisfying $q_e < 0$, with water vapor and rainwater explicitly included. It must be emphasized that the differences among DSI, CSI, and MSC are crucial in determining the stability of the descending motion.

d. Slantwise convective available potential energy (SCAPE)

The concept of convective available potential energy (CAPE) has been used by synopticians to identify regions favorable to upright convection. This energy is easily evaluated on a thermodynamic diagram from single-station radiosonde data. Emanuel (1983b) defines SCAPE similarly to CAPE but evaluates energy on an M surface

$$\text{SCAPE} = \int \frac{g}{\theta}(\theta_{\text{pa}} - \theta_{\text{en}})dl \qquad (2)$$

where θ_{pa} and θ_{en} are the parcel and environmental potential temperatures, respectively, and dl is the infinitesimal length along the M surface projected onto the vertical axis. The integration is done from the level of free convection to the level of nonbuoyancy. Although numerical simulations and analytical considerations show parcels moving nearly along the θ_e surface (Thorpe et al. 1989), this is not an essential point in the evaluation of SCAPE because the integral depends only on the extreme points of the path (Emanuel 1983b). In the development of parcel theory, it is implicitly assumed that the perturbation pressure forces are small and the environment will suffer minimal changes during the parcel displacement. For MSI the former hypothesis is reasonable because the parcel motion occurs approximately along a neutral buoyancy curve, while the latter is less easily justified, as we will show in section 4.

Emanuel (1983a) mentioned some mechanisms that change the value of SCAPE. It seems that any process acting to alter the difference between heights of the level of free convection and the level of nonbuoyancy along an M surface will alter the SCAPE. While differential horizontal ageostrophic advection can convert slantwise convection instability to upright convection conserving SCAPE, ageostrophic vertical advection can alter SCAPE. Irreversible processes like diabatic heating/cooling and surface friction will modify the SCAPE. It is interesting to note that although q_e and SCAPE must have opposite signs in a saturated atmosphere, a particular value of q_e does not correspond to one determined value of SCAPE. To show this, it is sufficient to present a mechanism capable of changing one quantity without affecting the other: a stretching motion along an M surface can decrease the gradient of θ_e along it, augmenting SCAPE. Since q_e is proportional to the solenoids formed by M and θ_e surfaces, this stretching must be compensated by a horizontal divergent motion advecting M, conserving the solenoids and q_e.

As will be shown later, a cold horizontal advection takes place above the surface in the colder sector. Since in our numerical simulations the potential temperature is kept constant and the horizontal velocity is imposed to be zero at the surface, a discussion about the effect of these assumptions on the SCAPE and q_e values will be useful in section 4 when the numerical results are presented. In this case the vertical mixing of heat will increase the potential temperature of the parcels above the surface, increasing the SCAPE. The frictional effect will also increase the SCAPE by making the M surfaces less tilted (according to Fig. 14 of Emanuel 1983a). The effect on q_e can be understood by evoking the first and second terms on the right-hand side of (1). The first term is proportional to $\nabla S_{\ominus e}$ along the vector $\underset{\sim}{\eta}$ and M surfaces. In the situation analyzed, the surface acts as a source of θ_e. Thus, this term is negative and decreases the value of q_e. The second term is proportional to

$$-\frac{\partial S_{my}}{\partial z}\frac{\partial \theta_e}{\partial x} + \frac{\partial \theta_e}{\partial z}\frac{\partial S_{my}}{\partial x}$$

where S_{my} represents sources and sinks of y momentum. Since the surface is a sink of y momentum when θ_e is increasing with the x axis, the first term above contributes to decreasing the value of q_e. In the case of convective stability, the contribution due to the second term will depend on the horizontal distribution of S_{my}.

3. The model formulation

a. Governing equations

We employ the primitive equations written in the two-dimensional form, with hydrostatic, anelastic, and quasi-Boussinesq approximations (the vertical derivative of the basic-state density is retained in the continuity equation).

Let θ and Π be the deviations of potential temperature and Exner function $\Pi \equiv c_p/(p/p_r)^{R/c_p}$ from a steady, neutrally stable reference state defined by $\Pi_0(z)$ and θ_0 constant in hydrostatic balance, where p is the pressure, p_r a reference pressure, R the specific gas constant for dry air, and c_p its specific heat capacity at constant pressure. The system of equations is given by the momentum equation, the hydrostatic relation, the mass continuity equation, the thermodynamic equation, and the conservation of vapor r_v, cloud r_c, and rain r_r specific mass. They are written in the form

$$\frac{\partial \mathbf{V}}{\partial t} + \frac{\partial u\mathbf{V}}{\partial x} + \frac{1}{H}\frac{\partial Hw\mathbf{V}}{\partial z} + f\mathbf{k}\times\mathbf{V} + \theta_0\nabla_h\Pi = \mathbf{S}_m \qquad (3)$$

$$-g\left(\frac{\theta}{\theta_0} + 0.608r_v - r_c - r_r\right) + \theta_0\frac{\partial \Pi}{\partial z} = 0 \qquad (4)$$

$$\frac{\partial u}{\partial x} + \frac{1}{H}\frac{\partial Hw}{\partial z} = 0 \qquad (5)$$

$$\frac{\partial a}{\partial t} + \frac{\partial au}{\partial x} + \frac{1}{H}\frac{\partial Hwa}{\partial z} = S_a, \quad a = \theta, r_v, r_c, r_r \qquad (6)$$

where $\mathbf{V} = (u, v)$ is the horizontal velocity vector; u and v the velocities along the x and y axis; w the vertical velocity along the z axis; g the acceleration of gravity; ∇_h the horizontal gradient operator; S_a the sources and sinks of θ, r_v, r_c or r_r; $\mathbf{S}_m$ the sources and sinks of momentum; and $H \equiv \Pi_0^{c_v/R}$. From Eq. (5) we can define the streamfunction for the transverse motion by $\partial\psi/\partial z = Hu$ and $\partial\psi/\partial x = -Hw$.

b. Microphysical parameterization

Since our intention here is to capture the feature distinguishing MSC from CSI, namely, the explicit inclusion of vapor and rain, a simple parameterization of the processes representing interactions between the variable θ, r_v, r_c, and r_r is used. The sources and sinks for cloud, vapor, rain, and potential temperature are given, respectively, by

$$S_c = A - B - D - E + T_c$$

$$S_v = -A + B + C + T_v$$

$$S_r = -C + D + E - F + T_r$$

$$S_\ominus = \frac{L}{\Pi}(A - B - C) + T_\ominus$$

where T_v, T_c, T_r, and $T_\ominus$ represent subgrid turbulent processes to be parameterized, L is the latent heat of condensation, and

A condensation rate of r_v
B evaporation rate of r_c
C evaporation rate of r_r
D autoconversion rate of r_c into r_r
E collection rate of r_c by falling raindrops
F loss of r_r due to precipitation.

The saturation mixing ratio r_s is computated from the Teten's formula given by Soong and Ogura (1973). The approximate net change of water vapor necessary to bring a parcel to saturation is given by

$$\Delta r_v = (r_v - r_s) \Big/ \left[\frac{bLr_s}{c_p(\theta\Pi/c_p - 36)^2} + 1\right]$$

where $b = 4092.8$, which is equal to $(A - B)$ when $\Delta r_v > 0$. In the case that $\Delta r_v < 0$, $(A - B) = \min(\Delta r_v, r_c)$. The collection follows the relation given by Klemp and Wilhelmson (1978), namely,

$$E = 2.2 r_c r_r^{0.875} \quad [\text{g g}^{-1}] \tag{7}$$

and any excess in r_c over a threshold value of 0.0005 g g^{-1} is autoconverted into r_r. Term F is given by $\partial(V_t r_r)/\partial z$, where V_t is the raindrop's terminal velocity, which is calculated from the simplified relation employed by Thorpe et al. (1982):

$$V_t = 21.179 r_r^{0.2} \quad [\text{m s}^{-1}]. \tag{8}$$

The rain evaporation rate is given by the relation

$$C = 0.2 r_r^{0.675}(r_s - r_v) \quad [\text{g g}^{-1}] \tag{9}$$

and will be kept equal to zero whenever $r_v \geqslant r_s$. Equation (9) gives results similar to the parameterization used by Klemp and Wilhelmson (1978).

c. Boundary conditions, subgrid-scale parameterization, and grid system

The grid system is a staggered C grid, as defined by Messinger and Arakawa (1976). At the lower boundary a no-slip condition is used, and at the upper boundary a stress-free condition is employed. The pressure at the upper boundary is adjusted geostrophically to the velocity v in each time step. At the lateral boundaries radiational conditions, as suggested by Orlanski (1976), are used for the prognostic variables u and v. For θ, a null horizontal eddy transport condition gave better results. The vertical velocity is zero at the lower boundary and is calculated at the upper boundary. The potential temperature is fixed at the lower boundary.

In addition to the physical necessity of representing the subgrid eddy transports, there is a numerical requirement to control the accumulation of energy in the two gridpoint wavelength, caused by the nonlinear aliasing effect. For that, we use the simplest K theory for horizontal and vertical diffusion.

d. Domain and numerical procedures

The domain has a horizontal extension of 560 km represented by 40 grid points, with grid length $\Delta x = 14$ km. In the vertical, $\Delta z = 300$ m and the depth is 7.5 km. The time differencing scheme is leapfrog for the advective terms and forward for the diffusion terms with a time increment of $\Delta t = 30$ s. An Asselin time filter is used to prevent the separation of solutions inherent to the leapfrog scheme. Second-order approximation is used to calculate spatial derivatives.

In each time step, we first calculate the evolution of all variables considering only advective and diffusion terms. Afterwards, the microphysical parameterization is performed and the supersaturation is removed. If a grid point is subsaturated and there is some cloud water present, the cloud water is evaporated until the grid point becomes saturated. The advection of r_r due to precipitation (term F) is calculated following the scheme proposed by Smolarkiewicz (1983). This procedure prevents the rain mixing ratio from becoming negative. Further details about the numerical model can be found in Innocentini (1986).

4. Numerical experiments

The discussion of MSC is based on four simulations. The focus will be on the importance of humidity distribution in the water budget accompanying the development of MSC and the factors affecting the displacement and maintenance of the updraft.

a. Initial condition

The initial condition must be the simplest possible in order to enable understanding of the basic mechanism of MSC. The θ and v fields are initialized to satisfy the thermal wind balance. The vertical eddy diffusion coefficients are 8 $m^2 s^{-1}$, except for v and θ, where a small vertical variation is permitted to allow the initial condition to represent a steady equilibrium; that is, the eddy transports of heat and momentum are constant in the z direction, instead of the diffusion coefficients as is usually assumed in the K theory. The horizontal eddy diffusion coefficient is 4000 $m^2 s^{-1}$. Other requirements are that the equivalent Ertel potential vorticity and relative humidity be nearly uniform along each horizontal level to avoid the displacement of MSC toward some particular region in the domain due to nonhomogeneous horizontal distribution of these fields. Later, the atmosphere is made drier in some sectors of the domain in order to explore the effect of humidity alone on the unstable motion. Also, an initial condition satisfying the CSI criterion, but free of upright and inertial instabilities, is desirable to enhance the physical insight on MSC.

The initial fields satisfying these requirements are difficult to obtain due to the complexity of the equations involving water substance. The simple initial condition used by BH, ST87, and Sun (1984), consisting of constant vertical geostrophic shear, gives a slight tendency to decrease the vertical gradient of θ_e on the warm side of the domain when an uniform relative humidity is assumed. This causes a nonuniform horizontal distribution of buoyant stability and q_e. We chose instead to specify a constant horizontal gradient of θ_e. Figure 1 shows the initial fields of M, θ, θ_e, RH, and q_e. Although observational studies do not evidence so large an area with $q_e < 0$, this initial field will be useful for understanding the basic dynamic imposed by MSC.

Following Emanuel (1983b), the SCAPE released by a parcel displacement is given by (2). Along a general path it is

$$\text{SCAPE} = \int_{\text{SLFC}}^{\text{SLNB}} \left[f(M_{\text{pa}} - M_{\text{en}})\mathbf{i} + \frac{g}{\theta}(\theta_{\text{pa}} - \theta_{\text{en}})\mathbf{k} \right] \cdot d\mathbf{s} \quad (10)$$

where SLNB and SLFC are the levels of slantwise nonbuoyancy and free convection, respectively. Since SCAPE is not dependent on the path, but only on its extreme points, this quantity is easily obtained on a thermodynamic diagram when the chosen path is an M surface, and Eq. (10) is reduced to Eq. (2).

Figure 2 presents a sounding of the initial θ and dewpoint along the M surface 50 m s^{-1}. If any parcel in the saturated layer (920–690 mb) is lifted along the M surface, it will have positive buoyancy. The SCAPE

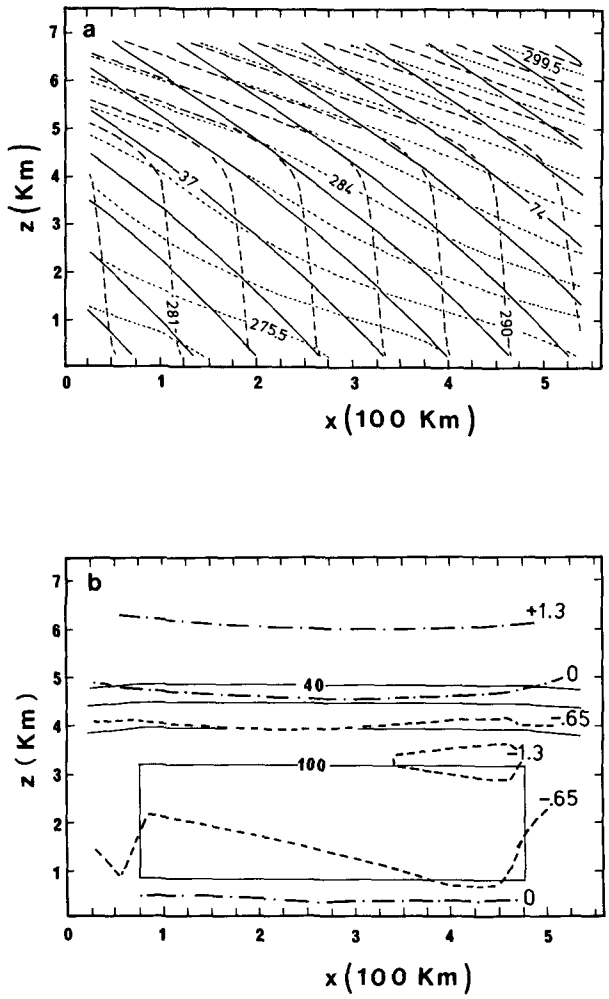

FIG. 1. Initial condition for the numerical simulations. (a) Potential temperature (in K, dotted lines), equivalent potential temperature (broken lines), and M (in m s^{-1}, solid lines); (b) Relative humidity (in %, solid lines) and equivalent Ertel potential vorticity [in 10^{-7} K (m s)$^{-1}$, broken and broken-dotted lines].

of a parcel originally at 920 mb is 297.8 $m^2 s^{-2}$, meaning that this parcel would have a velocity of 24.4 m s^{-1} at 400 mb in the absence of frictional forces. However, the simulations performed show that the parcel takes more than 20 hours to get to this level, and it seems unreasonable to neglect frictional forces and turbulent processes for so long a time period. Keeping in mind that SCAPE does not depend on the path when the environmental properties are not modified and our simulations show parcels moving nearly parallel to θ_e surfaces, it is instructive to compute the parcel velocity also along this surface.

Figure 3 shows the velocity of a parcel moving along the M surface 50 m s^{-1} and θ_e surface 289 K while the SCAPE is released. Note that for levels below about 5600 m the velocity computed along the M surface is higher (as analytically shown by Emanuel 1983b). In

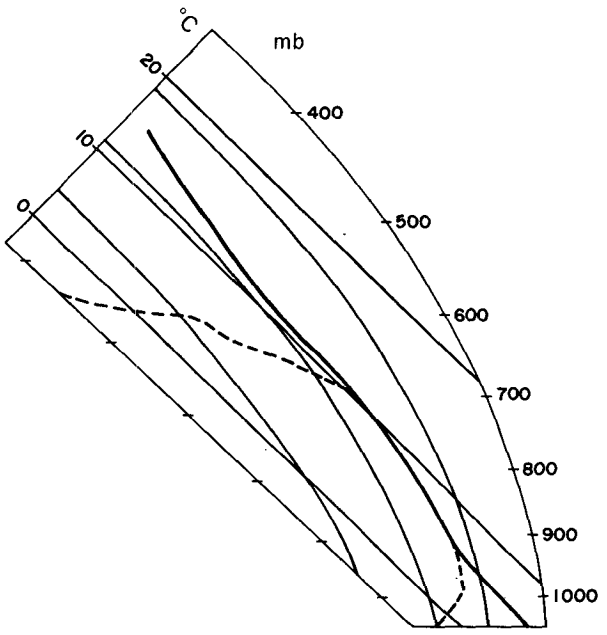

FIG. 2. Sounding along the M surface 50 m s^{-1} on a skew T-log$p$ diagram. The full line is the temperature, and the broken line the water vapor mixing ratio. Thin lines represent adiabatic and pseudoadiabatic processes.

the next section, velocities determined by the parcel theory and those obtained by the numerical experiments will be compared.

b. *The experiments*

The initial field must be perturbed in order to release SCAPE. Note that a perturbation on the transverse circulation, (i.e., u and w) is desirable because it affects neither the initial equivalent potential vorticity q_e nor the SCAPE. Several configurations of u and w satisfying the continuity equation were applied, showing that they are very important in determining the development of slantwise convection. Also, considerable computer time can be saved, due to earlier triggering of the unstable motion, when the initial updraft slope is nearly parallel to θ_e surfaces and a small cloudy area is included along the updraft. Figure 4 shows the streamlines and the cloudy area used in the initial condition. The contour interval value was divided by H at the surface equal to $1007^{2.5}$. The maximum vertical and horizontal velocities imposed by the initial perturbation is 13.6 cm s^{-1} and 1 m s^{-1}, respectively. The cloud-water mixing ratio is 0.1 g kg^{-1}, which is much less than the threshold value of 0.5 g kg^{-1} necessary to start the precipitation.

The experiments are summarized in Table 1. Experiment E1 is the control experiment. Experiment E2 was designed in order to compare the effect of evaporation on the downdraft with E1, and experiment E3 is intended to show effects on the updraft and downdraft intensities when water vapor is removed from the initial fields pictured in Fig. 1. The relative humidity is dropped to 50% in the sector of the domain arising in the left side of the initial updraft. Experiment E4 is identical to E3, except that the relative humidity is dropped in the right side of the initial updraft. The objective of E4 is to investigate the influence of drier air in the warm sector on the development of MSC when SCAPE at initial stages is not present in that region.

c. *The basic updraft dynamic*

An understanding of the dynamics of CSI can be obtained from the evolution of the ageostrophic wind

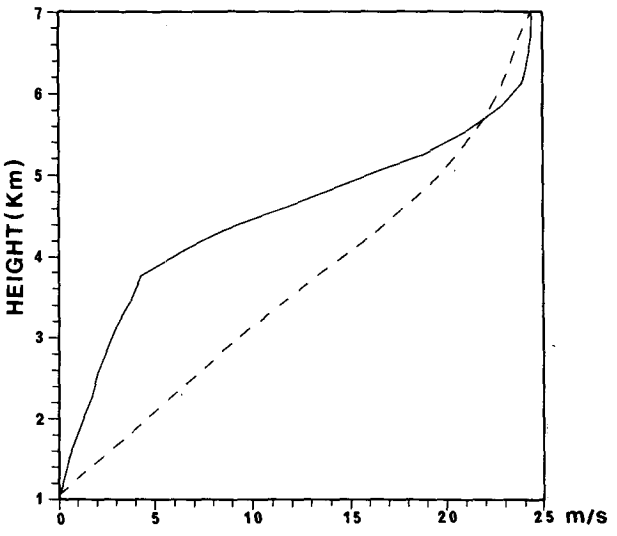

FIG. 3. The transverse velocity to the thermal wind vector in m s^{-1} based on the SCAPE. The broken line is along the M surface 50 m s^{-1}, and the solid line along the θ_e surface 289 K.

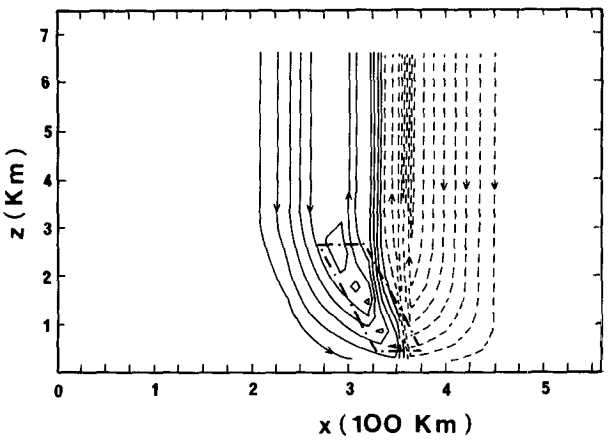

FIG. 4. Streamlines of the initial perturbation and cloudy area. The dashed line represent negative value for the streamfunction. The broken-dotted line bounds the cloudy region. The contour interval is 8.1 m^2 s^{-1}.

TABLE 1. Summary of the main characteristics of the numerical experiments.

Experiment	Main features
E1	All microphysical processes are considered and initial condition as in Fig. 4
E2	Like E1, except that the rain evaporation is not considered
E3	Like E1, except that the initial condition is drier in the left side of the initial updraft
E4	Like E1, except that the initial condition is drier in the right side of the initial updraft

component v_a along the thermal wind vector. It is given by

$$fv_a = fv - \theta_0 \frac{\partial \Pi}{\partial x} \tag{11}$$

and contributes to the transverse velocity, neglecting the effect of friction, by

$$\frac{Du}{Dt} = fv_a. \tag{12}$$

In our simulations, initially the ageostrophic force fv_a is zero, and the pressure force $-\theta_0 \partial \Pi / \partial x$ is negative (i.e., the pressure increases with x). The advection of M and θ and condensation of water vapor will destroy this geostrophic balance, accelerating the transverse velocity u. We will analyze how this evolves when a weak and well-defined updraft already exists (shown in Fig. 5) and the nonlinear effects are small. The updraft slope is steeper than M surfaces. This means that a negative M advection works to decrease locally the value of fv. This effect itself accelerates parcels in the region of the developing updraft toward the direction of decreasing x.

Along the updraft, θ_e surfaces are slightly steeper than streamlines. Thus, the motion has positive advection of θ_e and increases locally the value of θ_e (and θ as well, since RH = 100% in the updraft). The effect on the pressure will depend on the boundary condition imposed in the hydrostatic model. In our case, the upper-level pressure change is assumed to be in geostrophic balance, and at initial stages its time variation is very small. Then the warming accompanying this ascending motion decreases the pressure, most intensely in the central part of the updraft where the velocity is strongest and the condensation is greatest. Therefore, this contribution to the horizontal pressure gradient is negative (positive) on the left (right) half of the updraft.

The combination of the advective effects of M and θ_e will determine the acceleration of velocity u [Eq. (12)]. On the right half of the updraft both effects tend to make fv_a negative, while on the other half they have opposing contributions. Since the motion is almost parallel to θ_e, the advection of this quantity serves only to reduce the tendency determined by the advection of M on the left half of the updraft and reinforce it on the other half. Thus, there is a small tendency for the updraft to move toward the warmer side of the domain, while parcels themselves move toward the colder side. Note that if the pressure were imposed to be constant at the surface, the updraft would drift toward the colder region. This analysis contrasts with the linear theory by Ooyama (1966) where the modes are free in an unbounded domain, resulting in no phase velocity.

d. The E1 experiment results

Figure 5 shows the streamlines and the contours RH = 100% at t = 6, 12, 18, 24, and 30 h. Two cellular structures can be observed with a relatively intense sloped updraft between them, drifting slowly toward the warmer side (as predicted by the preceding qualitative discussion) with a velocity of about 4.5 km h^{-1} at low levels, and slightly less at higher levels. In agreement with this result, ST87 also shows a slantwise updraft displacing toward the warmer sector with a velocity of 2.5 km h^{-1} (inferred from their Fig. 9). The RH becomes less than 100% except within the updraft. The two cells present comparable structure up to t = 12 h, but after that the counterclockwise cell is intensified because the sloped descending motion becomes unstable in the rainy area due to the rain evaporation. This factor emphasizes the distinction between MSC and CSI. At t = 24 h the sloped updraft is in its more vigorous stage, shaping a wide streak of horizontal velocity higher than 9 m s^{-1} (maximum negative u value is 10.4 m s^{-1} at x = 245 km and z = 4.7 km) and vertical velocity of 15 cm s^{-1} (maximum w value is 17.4 cm s^{-1} at x = 322 km and z = 3 km). The descending motion has maximum horizontal and negative vertical velocities of 6.1 m s^{-1} at x = 245 km and z = 3.6 km, and 9.8 cm s^{-1} at x = 287 km and z = 2.7 km, respectively. Note that at t = 30 h two secondary cells develop at low levels near x = 100 km and x = 250 km. They are created by upright instability generated probably by the destabilizing effect of evaporative cooling aloft combined with a small negative θ advection. These cells, however, are unrealistically simulated since the inclusion of the hydrostatic assumption into the two-dimensional model may no longer be valid at this later stage.

Figure 6 presents trajectories of a few selected parcels computed by linear interpolation of velocities. The parcel represented in Fig. 6a is captured by the strong updraft at t = 12–18 h and is pushed out of the domain at about t = 30 h. Figure 6b shows a parcel initially located about 50 km from the parcel in Fig. 6a. Up to t = 12 h, the parcel is in the updraft, which is moving toward the right side. By t = 18 h it reaches the downdraft region and returns to nearly its original horizontal level. The parcel in Fig. 6c is captured by the same downdraft at t = 12–18 h, and is brought down to levels near the surface relatively quickly. From these

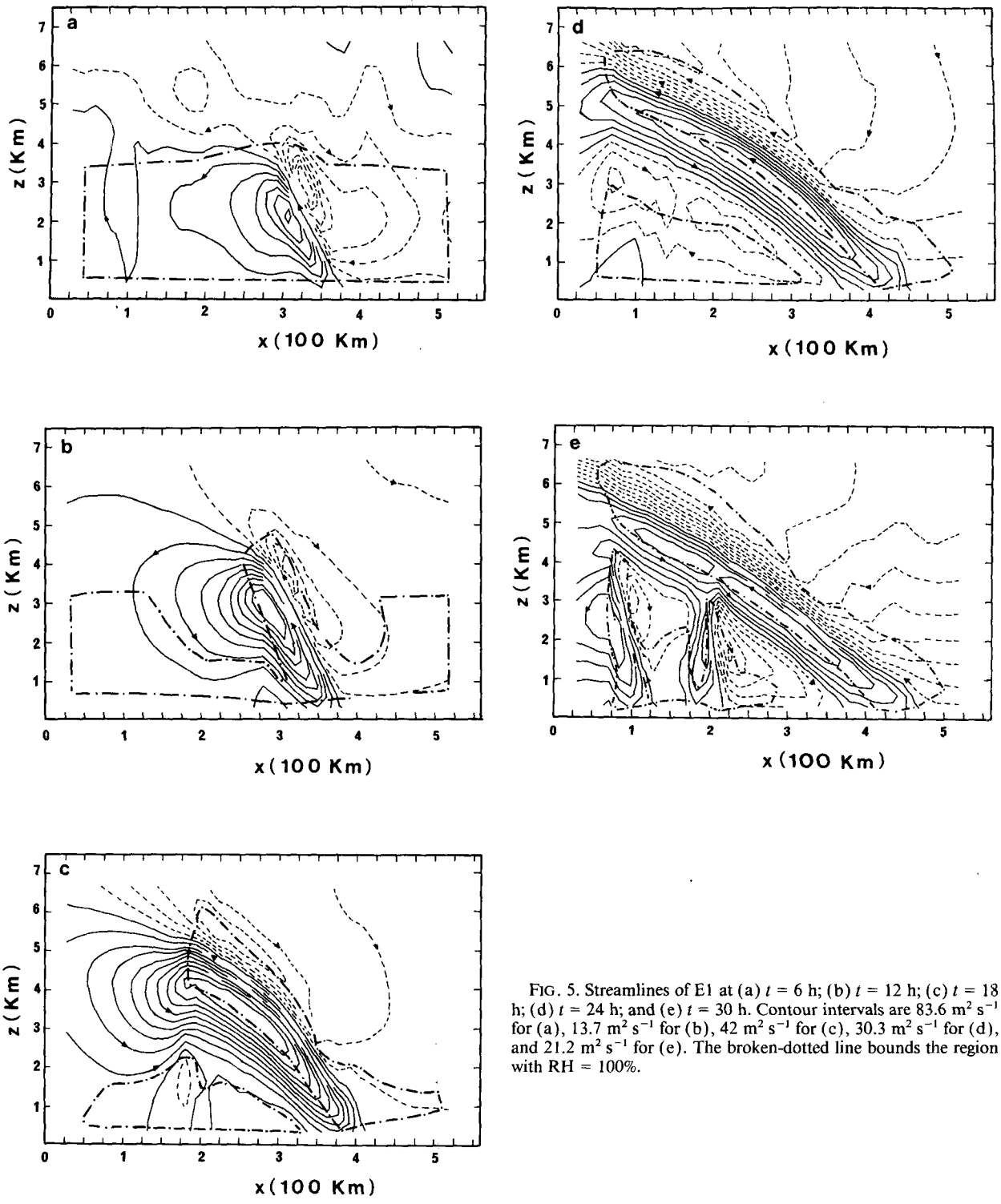

FIG. 5. Streamlines of E1 at (a) $t = 6$ h; (b) $t = 12$ h; (c) $t = 18$ h; (d) $t = 24$ h; and (e) $t = 30$ h. Contour intervals are 83.6 $m^2 s^{-1}$ for (a), 13.7 $m^2 s^{-1}$ for (b), 42 $m^2 s^{-1}$ for (c), 30.3 $m^2 s^{-1}$ for (d), and 21.2 $m^2 s^{-1}$ for (e). The broken-dotted line bounds the region with RH = 100%.

analyses, it is clear that parcels on the warmer side to the right of the initial imposed updraft are captured by the updraft. Eventually, parcels initially in the updraft leave it and enter the descending motion branch.

As mentioned before, the maximum u velocity occurred at $z = 4.7$ km. An inspection of Fig. 3 shows that a parcel moving along a θ_e surface should have at this level a velocity of 14 m s^{-1}. This indicates that

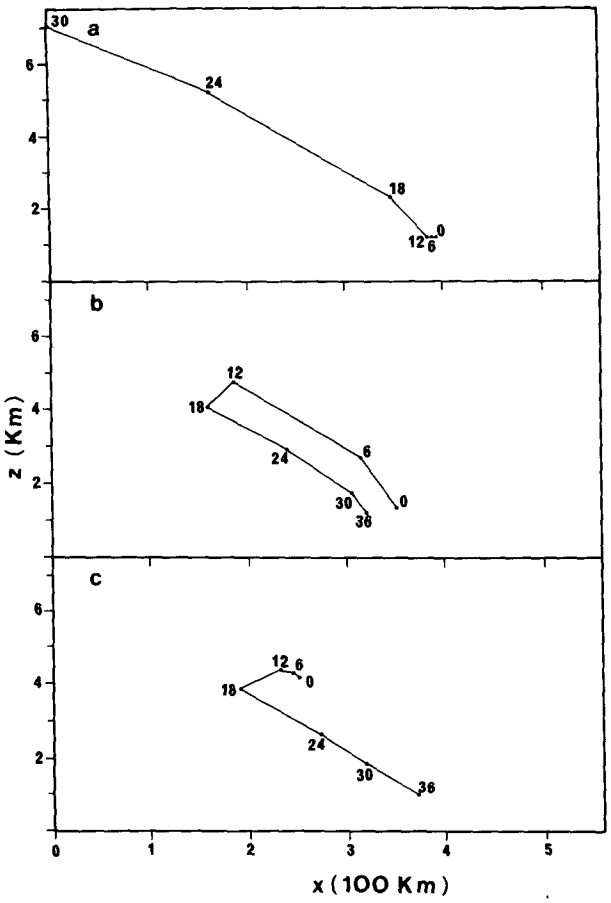

FIG. 6. Trajectories of a few selected parcels. The numbers indicate the time position (in hours) of the parcels.

roughly only 55% of the SCAPE available for a parcel coming from lower levels was effectively used to accelerate the parcel.

e. *Effect of slantwise convection on the experiment E1 initial field*

While the motions resulting from MSC are evolving, M and θ are advected and modified by turbulent processes, exhibiting different configurations from those initially imposed. The changes produced in $\partial M/\partial x$, $\partial\theta/\partial z$, $\partial\theta_e/\partial z$, and q_e are of interest in determining how inertial, dry/moist, upright, and symmetric instabilities develop.

At $t = 24$ h, the shaded areas in Figs. 7a,b represent regions unstable to dry and potentially unstable to moist upright motions, respectively. Note that the small dry unstable region (Fig. 7a) is near the surface and appears to be due to the boundary condition assumed. Certainly a better vertical turbulent mixing might prevent the generation of this instability. Although the regions with moist buoyant instability are very large, little unstable motion is triggered because RH is less than 100% except within the updraft. The unstable area above the updraft is coupled with the descending motion imposed by the subsaturated clockwise cell and therefore, is not favorable for allowing the development of convection. These instability criteria are expected to appear above the region of maximum warming (i.e.,

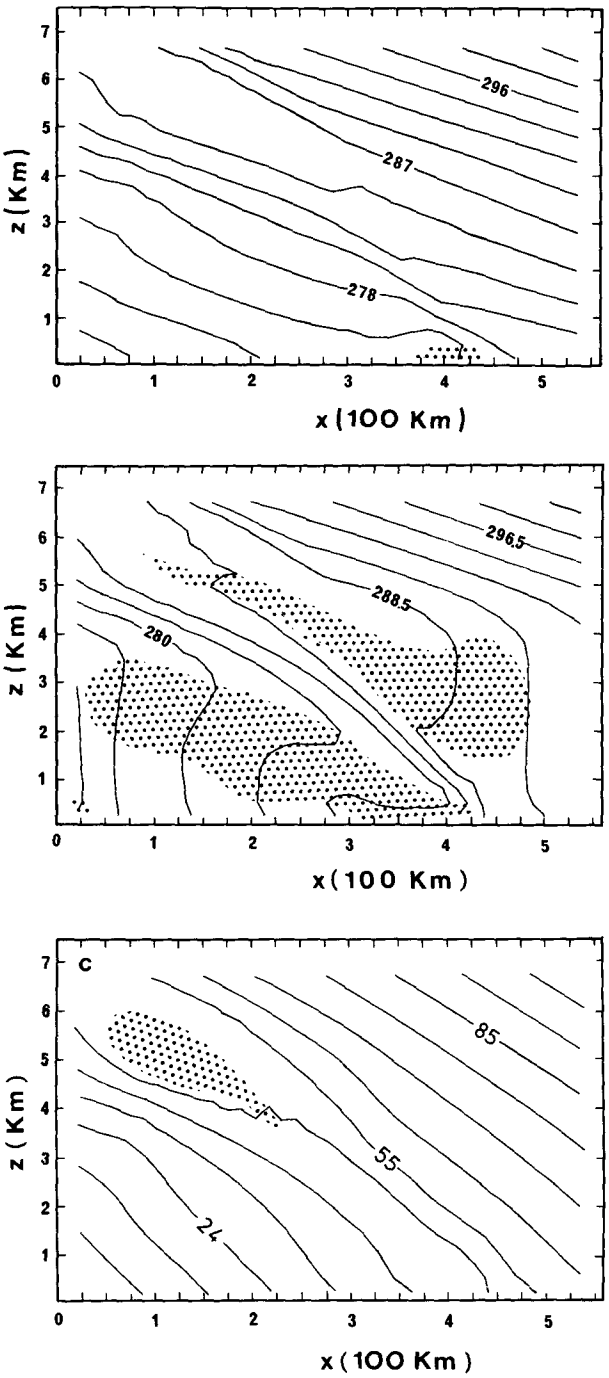

FIG. 7. Fields of experiment E1 at $t = 24$ h: (a) θ (K), (b) θ_e (K), and (c) M (m s^{-1}). The shaded area represents $\partial\theta/\partial z < 0$ in (a), $\partial\theta_e/\partial z < 0$ in (b) and $\partial M/\partial x < 0$ in (c).

above the sloped updraft) where there is a maximum positive advection of θ_e. The negative θ_e advection in the descending motion is very effective in generating potential upright instability in a large low-level area, where intense vertical motion develops after $t = 24$ h, as presented in Fig. 5e. The ST87 simulation also shows an unstable region above the updraft, but in contrast a strong upright stabilization appears, with $Ri_e > 1$, below the updraft, which prevents the development of any vertical circulation.

Figure 7c shows small shaded regions at $t = 24$ h where inertial instability ($\partial M/\partial x < 0$) has developed. A region of inertial instability (not shown) accompanies the slanted updraft on the upper part of its left side, during the model integration period. As a consequence, a well-defined jet along a thermal wind direction is generated in that region, caused by positive advection of M. By comparing Figs. 7b and 7c, the M and θ_e surfaces are approximately parallel within the region where the strong up and down slantwise motion develops. This means that SCAPE is nearly zero along this region.

In large-scale numerical models, convective transports are subgrid processes that must be parameterized due to the inability of explicit simulation. Presently, most of these models have a horizontal grid length of 100–200 km, and therefore even mesoscale processes ranging from 20 km to 200 km, such as moist slantwise convection, must also be parameterized. There is no intention here to suggest any parameterization scheme for MSC in a large-scale model. But it is useful to show how several average initial fields are modified by it.

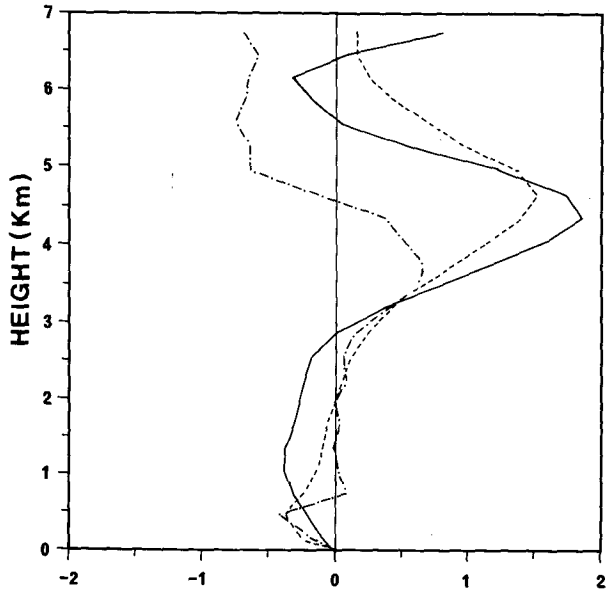

FIG. 8. Horizontally averaged deviation from the initial condition at $t = 24$ h of longitudinal velocity v (in m s^{-1} and continous line), potential temperature θ (in K and broken line), and equivalent potential vorticity q_e [in 10^{-7} K (m s)$^{-1}$ and broken-dotted line].

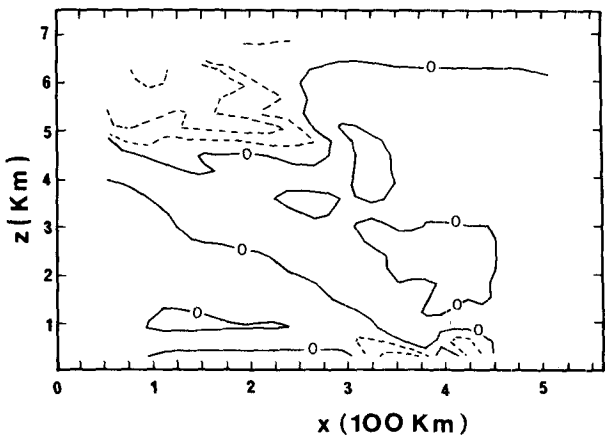

FIG. 9. Deviation of equivalent potential vorticity q_e at $t = 24$ h from $t = 0$ h. Dashed (full) lines represent negative (positive) contours. The zero contours delimitate positive and negative deviation. Contour interval is 1.01×10^{-7} K (m s)$^{-1}$.

The deviation from the initial condition of velocity v and potential temperature at $t = 24$ h is averaged at each level and plotted on Fig. 8. The velocity v decreases near the surface due to the quasi-horizontal negative advection of M by the counterclockwise cell. Along the slanted updraft, there is also negative advection of M. At higher levels, the strong quasi-horizontal motion driven by inertial instability advects greater M from the right, increasing the value of v and generating the upper-level along-thermal wind jet as mentioned earlier. The evaporative cooling and negative advection decrease θ at low levels, while the heat release by condensation on the updraft increases it at higher levels. Near the top, the overshooting of dry air by the upper part of the clockwise cell decreases the temperature.

Figure 8 also shows the deviation of q_e from the initial condition averaged at each horizontal level at $t = 24$ h. Three distinct layers are evident: a lower layer (LL), from $z = 0$ to $z = 2.0$ km, where the time variation of q_e is negative or nearly zero; a middle layer (ML) from $z = 2.0$ to $z = 4.5$ km with positive variation; and a higher layer (HL) with negative variation. In the LL the surface effects are very important in decreasing q_e, as discussed in section 2. In the ML the mixing processes in the slanted motion destroying the initial $q_e < 0$ are visible in the averaged q_e. The HL was initially a region with $q_e > 0$, and the advection transporting $q_e < 0$ from ML decreases q_e in this layer.

This discussion can be better illustrated by Fig. 9, which shows the domain deviation of q_e at $t = 24$ h from that imposed on the initial condition. Note the negative advection of q_e from the ML to HL, while in the LL q_e is decreasing due to surface effects near $x = 350$ km. An increase of q_e is also detected in the ML along the slantwise motion region.

Figure 10 shows the v velocity deviation at $t = 24$ h from $t = 0$ h at each grid point. Note that at high levels

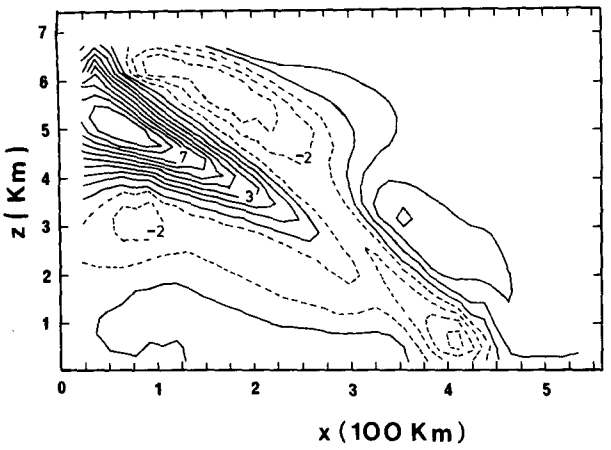

FIG. 10. Deviation of the v velocity (m s^{-1}) from the initial condition at t = 24 h. Contour interval is 1 m s^{-1}.

along the updraft, the v velocity is decreased, and increased along the downdraft. Near the surface the quasi-horizontal motion advects parcels with small M near x = 400 km from the left, decreasing the local value of v. The increase of velocity caused by the inertial instability as shown in Fig. 7c generates a strong high-level jet on the left of the updraft at z = 5 km. This result was not observed in the simulation of ST87, ST88, and BH, although the latter has pointed out a similar inertial instability region in their experiment. Ahead of the updraft there is an indication of a weak low-level jet about 2–3 km in height. The horizontal gradient of the v velocity at $x \approx 100$ km and $z \approx 5$ km is 11 m s^{-1}/(100 km), and the vertical gradient at $x \approx 400$ km and $z \approx 1.5$ km is about 7 m s^{-1}/(1 km).

f. Comparison between experiments

The relevance of the rain evaporation and water vapor availability on the water regime can be evaluated from Fig. 11. It shows the domain-integrated cloud and rain and the accumulated precipitation as a function of time, for experiments E1–E4. Note that the cloud mass amount in the atmosphere (represented by solid lines) is similar in E1 and E3, and smaller in E2 and E4. The experiment E2 (with no rain evaporation) shows a much higher amount of precipitation (represented by broken lines) during the first 24 h because all the rain produced falls out without evaporating. Experiments E1 and E3 show a tendency to increase the precipitation after t = 24 h, due mainly to the presence of upright convective cells that develop beneath the sloping downdraft at the colder side as mentioned in the discussion of E1 experiment.

The importance of water vapor on the warmer side of the domain is evident by comparing experiments E3 and E4. The former experiment shows larger cloud, precipitation, and rain amounts. As suggested by the previous trajectory analysis, parcels on the warmer side feed the sloped updraft, and it is crucial that they contain a high water vapor concentration. It should also be noted that the precipitation amount in E3 is enhanced compared to its value in E1. Because the air underneath the updraft is drier, a more intense evaporation occurs. This generates a more intense downdraft (the velocities are approximately 10% stronger than in other experiments). Thus, a much stronger mass convergence near the surface is produced that forces the sloped updraft.

Figure 12 shows the one-hour cumulative precipitation in each grid point for all experiments. The first interesting characteristic is the drifting to the warmer side of the sloped updraft in experiments E1 and E3 in contrast to experiments E2 and E4. The maximum vertical velocity values at z = 900 m at each 6-h interval (denoted by black circles) are also shown for all experiments. The results suggest the major roles played by the moisture contents and evaporation on the evolution and intensity of MSC. The experiment E4 shows clearly that the drier air on the warmer sector inhibits the development and any drifting of a well-defined sloped updraft. On the other hand, the evaporation effect acts directly on the sloped updraft intensity and consequently on the updraft drifting (experiment E2 shows a smaller displacement than experiments E1 and E3). Note that in E2 and E4 a smaller availability of water vapor and/or a smaller convergence at low levels seems to be decisive in preventing the triggering of the convective unstable motion, as observed in experiments E1 and E3. These unstable regions produce after 24 h a more intense precipitation associated with the strong vertical circulation generated in those regions, as shown in Fig. 12, but as discussed earlier they are unrealistically simulated. The other two precipitation areas occur in E1 and E4 on the left boundary, caused probably by the boundary condition assumed.

The maximum accumulated rain in a 24-h simulation is 3.1 mm in experiment E3 near x = 340 km. This is a reasonable value when a hydrostatic condition is assumed. For example, a saturated air ascending with a velocity of 30 cm s^{-1} (an upper limit under hydrostatic approximation) in a 1-km-thick layer would produce approximately 40–50 mm of rain in 24 h. In our simulation the vertical velocity neither reaches that upper value nor is concentrated in a fixed region for so long a time period.

5. Summary and conclusions

A two-dimensional hydrostatic primitive equation numerical model is used in order to simulate MSC in an atmosphere with initial CSI. Although only simplified cloud microphysics is incorporated, the model was able to produce a well-defined slanted updraft with horizontal velocity greater than 10 m s^{-1} perpendicular to the thermal wind vector. The slanted updraft has horizontal and vertical scales of 400 km and 6 km, respectively.

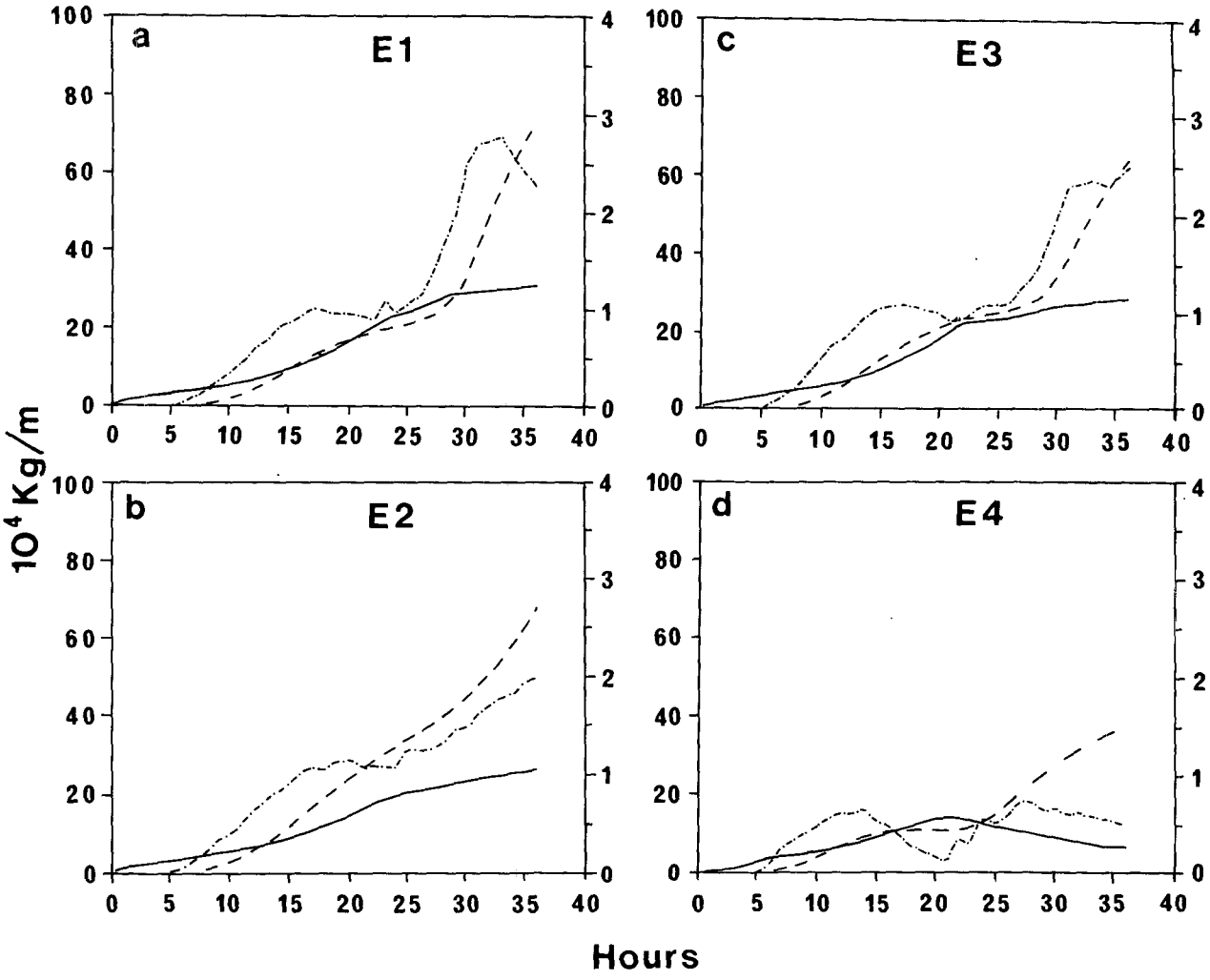

FIG. 11. The total accumulated precipitation (broken line, left panel), cloud (solid line, left panel), and rain (broken-dotted line, right panel) in the atmosphere as a function of the time, for (a) E1; (b) E2; (c) E3; and (d) E4.

The four numerical experiments conducted exhibit, after 5–10 h of time integration, a slantwise updraft oriented between the initial M and θ_e surfaces but closer to the latter, surrounded by two broader descending motions taking the form of two transverse rolls. The inherent advection acts on the initial field through ageostrophic forces in order to maintain the updraft. The roll in the warmer side has weaker velocities and feeds moist parcels at low levels into the updraft. At the same time, the updraft drifts toward the warmer region, overtaking the low-level moist parcels necessary for self-maintenance. The experiment with lower water vapor mixing ratio on the colder side (experiment E3) evidences the crucial importance of moister parcels on the warmer region feeding the updraft at low levels.

An enhanced roll in the colder side shows the difference between MSC and CSI. The roll in the warmer side tends to disappear as soon as the rain evaporation takes place. This seems to be supported by observations where no evidence of a warmer-side roll has been reported. The experiment without the rainwater evaporation (E2) shows the importance of this effect on the advance of the slanted updraft toward the warmer side. This advance is very important for feeding the updraft with moister and warmer parcels.

The SCAPE suggested by Emanuel (1983a) estimated a velocity about 50% greater than that obtained in our numerical simulation. The discrepancy may be partially explained by the neglect of mixing processes and water loading in the SCAPE theory. Also, the time required to lift a parcel from the surface to 4 km is more than 15 h, and the environmental properties around the region where the updraft are taking place are greatly modified, altering the SCAPE evaluated with the initial fields.

The horizontally averaged equivalent Ertel potential vorticity q_e shows that the condition of instability ($q_e < 0$) becomes less negative in the layer where slantwise

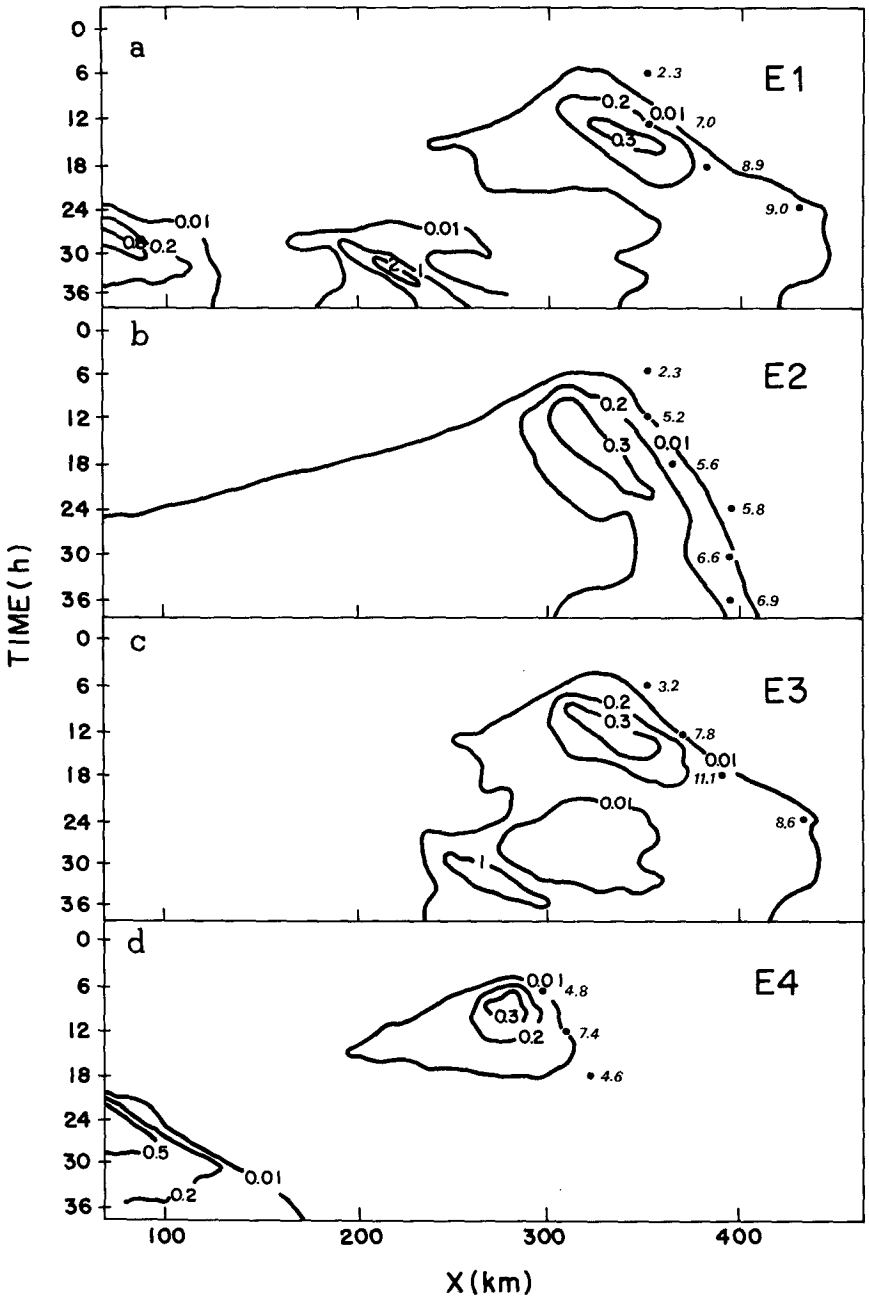

FIG. 12. Precipitation (in mm) produced during 1 hour at each grid point, for experiments (a) E1; (b) E2; (c) E3; and (d) E4. Black circles represent the location of the maximum vertical velocity (in cm s^{-1}) at each 6-h interval.

motions develop. However, a closer examination reveals that q_e remains negative in several parts of the domain, but new slanted updrafts will hardly occur due to the reduction of relative humidity and absence of any triggering mechanism. At high levels the initial $q_e > 0$ is reduced by advection of the parcels from lower levels with $q_e < 0$. The surface effects decrease q_e in that region. However, this reduction is not essential to maintain the updraft. The humidity content of parcels on the warmer side is crucial to maintain the updraft, and dryness on the colder side also has a strong positive role.

The unstable slanted descending motion below the updraft (in the sense of MSC) does not extend to the surface, so that a differential advection of θ occurs in this region. This effect implies the generation of po-

tential vertical instability, which was triggered in some simulated cases after t = 24–30 h, when the main updraft became weak. In this respect it is interesting to note the similarity between our Fig. 7b and Fig. 6a shown by Emanuel (1983a). His figure also presents a region with potential vertical instability that seems to be caused by a strong, cold slanted downdraft.

The circulation that developed in our experiment E1 shows a slanted updraft resembling in some aspects the warm conveyor belt of an anacold front described by Browning (1985). The ascending branch of the circulation is warm and moist, while the descending branch is dry and cold. Our model also suggests the generation of a low-layer weak jet on the warmer side. At higher levels the positive advection of M contributes to strengthening of the velocity along the thermal wind vector, generating a strong jet on the colder side in contrast with Browning's model.

Since most of the cases related with MSC presented by Emanuel (1983a,b), Sanders and Bosart (1985), Lemaitre and Testud (1988), and Browning's warm conveyor belt show rainbands in situations associated with frontogenetical forcing, we suggest for future research MSC experiments coupled with that forcing. Such experiments will extend the results of Emanuel (1985) and Thorpe and Emanuel (1985) by revealing new details. Both studies were limited to the elliptic Sawyer–Eliassen equation, which does not permit $q_e < 0$ because the geostrophic momentum approximation involved in its derivation breaks down.

Acknowledgments. The authors thank A. J. Thorpe, B. J. Hoskins, and R. P. Pearce, from University of Reading, who pointed out to one of us the importance of this study. Their assistance and valuable discussion gave us encouragement. We thank especially one referee and V. B. Rao, from INPE, for their useful comments, suggestions, and criticisms of early drafts of this paper.

REFERENCES

Austin, P. M., and R. A. Houze, 1972: Analysis of the structure of precipitation patterns in New England. *J. Appl. Meteor.*, **11**, 926–935.

Bennetts, D. A., and B. J. Hoskins, 1979: Conditional symmetric instability—a possible explanation for frontal rainbands. *Quart. J. Roy. Meteor. Soc.*, **105**, 945–962.

——, and J. C. Sharp, 1982: The relevance of conditional symmetric instability to the prediction of mesoscale frontal rainbands. *Quart. J. Roy. Meteor. Soc.*, **108**, 595–602.

Browning, K. A., 1985: Conceptual models of precipitation systems. *Meteor. Mag.*, **114**, 293–319.

——, and T. W. Harrold, 1969: Air motion and precipitation growth in a wave depression. *Quart. J. Roy. Meteor. Soc.*, **95**, 288–309.

——, and C. W. Pardoe, 1973: Structure of low-level jet streams ahead of mid-latitude cold fronts. *Quart. J. Roy. Meteor. Soc.*, **99**, 619–668.

Cunningham, R. M., 1951: Some observations of natural precipitation processes. *Bull. Amer. Meteor. Soc.*, **32**, 334–343.

Elliot, R. D., and E. L. Hovind, 1964: On convection bands within Pacific Coast and their relation to storm. *J. Appl. Meteor.*, **3**, 143–154.

——, and E. L. Hovind, 1965: Heat, water, and vorticity balances in frontal zones. *J. Appl. Meteor.*, **4**, 196–211.

Emanuel, K. A., 1983a: On assessing local conditional symmetric instability from atmospheric soundings. *Mon. Wea. Rev.*, **111**, 2016–2033.

——, 1983b: The Lagrangrian parcel dynamics of moist symmetric instability. *J. Atmos. Sci.*, **40**, 2368–2376.

——, 1985: Frontal circulations in the presence of small moist symmetric stability. *J. Atmos. Sci.*, **42**, 1062–1071.

Hobbs, P. V., 1978: Organization and structure of clouds and precipitation on the mesoscale and microscale in cyclonic storms. *Rev. Geophys. Space Phys.*, **16**, 741–755.

Houze, R. A., P. V. Hobbs, K. R. Biswas, and W. M. Davis, 1976: Mesoscale rainbands in extratropical cyclones. *Mon. Wea. Rev.*, **104**, 868–878.

Innocentini, V., 1986: Numerical simulations of moist slantwise convection. Ph.D. dissertation, University of Reading, 224 pp.

Jascourt, S. D., S. S. Lindstrom, C. J. Seman, and D. D. Houghton, 1988: An observation of banded convective development in the presence of weak symmetric stability. *Mon. Wea. Rev.*, **116**, 175–191.

Klemp, J. B., and R. B. Wilhemson, 1978: The simulation of three-dimensional convective storm dynamics. *J. Atmos. Sci.*, **35**, 1070–1096.

Lemaitre, Y., and J. Testud, 1988: Relevance of conditional symmetric instability in the interpretation of wide cold frontal rainbands. A case study: 20 May 1976. *Quart. J. Roy. Meteor. Soc.*, **105**, 945–962.

Messinger, F., and A. Arakawa, 1976: Numerical methods used in atmospheric models. GARP Publ. Ser. No. 17.

Nozumi, Y., and H. Arakawa, 1968: Prefrontal rainbands located in the warm sector of subtropical cyclones over oceans. *Rev. Geophys. Res.*, **73**, 487–492.

Ooyama, K., 1966: On the stability of the baroclinic circular vortex: A sufficient criterion for instability. *J. Atmos. Sci.*, **23**, 43–53.

Orlanski, I., 1976: A simple boundary condition for unbounded hyperbolic flows. *J. Comput. Phys.*, **21**, 251–269.

Saitoh, S., and H. Tanaka, 1987: Numerical experiments of conditional symmetric baroclinic instability as a possible cause for frontal rainband formation. Part I. A basic experiment. *J. Meteor. Soc. Japan*, **65**, 675–708.

——, and ——, 1988: Numerical experiments of conditional symmetric baroclinic instability as a possible cause for frontal rainband formation. Part II. Effects of water vapor supply. *J. Meteor. Soc. Japan*, **66**, 39–54.

Sanders, F., and L. F. Bosart, 1985: Mesoscale structure in the megalopolitan snowstorm of 11–12 February 1983. Part I: Frontogenetical forcing and symmetric instability. *J. Atmos. Sci.*, **43**, 1050–1061.

Sawyer, M., 1949: The significance of dynamic instability in atmospheric motions. *Quart. J. Roy. Meteor. Soc.*, **75**, 364–374.

Smolarkiewicz, P. K., 1983: A simple positive definite advection scheme with small implicit diffusion. *Mon. Wea. Rev.*, **111**, 479–486.

Solberg, M., 1936: Le mouvement d'inertie de l'atmosphere stable et son role dans le theorie des cyclones. Union Geodesique et Geophisique internationale VIeme assemblee, Edinburg, **Vol. II**, 66–82.

Soong, S. -T, and Y. Ogura, 1973: A comparison between axisymmetric and slab-symmetric cumulus cloud models. *J. Atmos. Sci.*, **30**, 879–893.

Sun, W. -Y, 1984: Rainbands and symmetric instability. *J. Atmos. Sci.*, **41**, 3412–3426.

Thorpe, A. J., and K. A. Emanuel, 1985: Frontogenesis in the presence of small stability to slantwise convection. *J. Atmos. Sci.*, **42**, 1809–1824.

——, M. J. Miller, and M. W. Moncrieff, 1982: Two-dimensional convection in non-constant shear: A model of mid-latitude squall lines. *Quart. J. Roy. Meteor. Soc.*, **108**, 739–762.

——, B. J. Hoskins, and V. Innocentini, 1989: The parcel method in a baroclinic atmosphere. *J. Atmos. Sci.*, **46**, 1274–1284.

Xu., Q., 1984: Conditional symmetric instability and mesoscale rainbands. Ph.D. dissertation, The Pennsylvania State University, 188 pp.